AIAA JOURNAL
Vol. 50, No. 10, October 2012

Development of a Mach 5 Nonequilibrium-Flow Wind Tunnel

M. Nishihara,* K. Takashima,* N. Jiang,* W. R. Lempert,† I. V. Adamovich,† and J. W. Rich‡
Ohio State University, Columbus, Ohio 43210
and
S. Doraiswamy§ and G. V. Candler¶
University of Minnesota, Minneapolis, Minnesota 55455

DOI: 10.2514/1.J051605

A small-scale Mach 5 blowdown wind tunnel has been developed to generate steady-state nonequilibrium flows. The wind tunnel uses transverse nanosecond pulse discharge, overlapped with transverse dc discharge, to load internal energy modes of N_2 and O_2 in plenum. The stable discharge is operated at high plenum pressures, at energy loadings of up to ~0.1 eV/molecule in nitrogen, generating nonequilibrium nitrogen and airflows with run time of 5–10 s, translational/rotational temperature of $T_0 \sim 300$–400 K, and N_2 vibrational temperature of up to $T_{V0} \sim 2000$ K. Internal energy-mode disequilibrium is controlled by injecting O_2, NO, H_2, or CO_2 into the subsonic flow between the discharge and the nozzle throat. Flow over a cylinder model in a Mach 5 test section is visualized by schlieren imaging and NO planar laser-induced fluorescence imaging, using a burst-mode laser operated near 226 nm, at a pulse-repetition rate of 10–20 kHz. NO planar laser-induced fluorescence images on two single-line NO($X, v' = 0 \rightarrow A, v'' = 0$) transitions are used to infer rotational temperature distributions in NO-seeded nitrogen flows in the supersonic section, with and without discharge. Single-line NO planar laser-induced fluorescence images on a NO($X, v' = 1 \rightarrow A, v'' = 1$) transition are used to infer the NO vibrational temperature in a nitrogen Mach 5 flow excited by the discharge and seeded with NO. The results are compared to three-dimensional nonequilbrium flow modeling calculations, showing good agreement.

I. Introduction

DEVELOPMENT of hypersonic flight technology requires extensive use of well-instrumented ground testing facilities, as well as predictive, physics-based modeling of nonequilibrium flows. One of the most critical problems with nonequilibrium flow characterization at large-scale, short-pulsed hypersonic facilities is limited ability to collect multiple data/image sets within the short run time (of the order of ~1 ms). Most optical diagnostics systems rely on pulsed lasers operating at fairly low pulse-repetition rates (of the order of ~10–100 Hz), which are only capable of taking a single "shot" (image or data set) per run. This restriction makes monitoring kinetic and fluid dynamic processes on a high-speed flow time scale (~1 μs) extremely challenging. This also severely limits the amount of data available for validation of nonequilibrium flow codes and for assessing their predictive capability outside the range of testing conditions on the ground. Therefore, development of high-frame-rate laser-diagnostics systems would dramatically enhance flow-characterization capability of pulsed hypersonic flow facilities. Development and extensive testing of such diagnostics requires a "test bed", laboratory-scale, steady-state, nonequilibrium flow facility.

Development of a wind tunnel producing well-characterized, steady-state, nonequilibrium hypersonic flows using controlled energy loading into internal (vibrational and electronic) molecular energy modes, as well as into molecular dissociation, is also of considerable interest. Such a facility would make possible studies of coupling between molecular energy storage, energy transfer, and flow characteristics. For example, delay of turbulent transition in a Mach 5 flow over a cone by means of injection of carbon dioxide into nitrogen or airflow has been recently demonstrated [1]. Kinetic modeling calculations [2] suggest that transition delay is caused by absorption of acoustic perturbations in the boundary layer by vibrational energy modes of carbon dioxide. Another example is relaxation of energy stored in internal degrees of freedom of molecules behind a bow shock, which may significantly increase shock standoff distance [3]. The presence of vibrationally and electronically excited species in a hypersonic flow may strongly affect emission signature from the shock layer. Finally, short-pulse electric discharges efficiently loading electronic energy levels of nitrogen and oxygen in air are currently being explored as means of hypersonic flow control, by producing repetitive localized pressure perturbations in the flow [4].

The present approach is to use a high-pressure, low-temperature, diffuse electric discharge sustained in the plenum of a small-scale supersonic wind tunnel to load internal energy modes of nitrogen and oxygen molecules. A similar approach has been used previously to develop electrically excited gas dynamic lasers [5–7] and to study feasibility of low-temperature MHD (magnetohydrodynamic) flow control [8–10]. Target nonequilibrium airflow parameters downstream of the discharge are as follows: run time at steady-state conditions 5–10 s, plenum pressure $P_0 \sim 0.5$–1.0 atm, translational/rotational temperature $T_0 \sim 300$–500 K, and vibrational temperature $T_{v0} \sim 2,000$ K. Internal energy-mode disequilibrium in the flow excited in the discharge can be controlled by injecting "rapid relaxer" species (carbon dioxide, nitric oxide, or hydrogen) into the subsonic nonequilibrium flow between the discharge section and the nozzle throat [11]. Nonequlibrium flowfield is studied in a steady-state flow over a cylinder model placed in a Mach 5 test section.

Optical diagnostics used in the present work includes schlieren imaging, UV/visible emission spectroscopy, and NO planar laser-induced fluorescence (PLIF) imaging using an OSU-developed burst-mode laser [12,13], which makes possible inference of

Presented as Paper 2010-1567 at the 48th Aerospace Sciences Meeting and Exhibit, Orlando, FL, January 4–7, 2010; received 26 September 2011; revision received 22 February 2012; accepted for publication 6 March 2012.

*Post-doctoral Researcher, Michael A. Chaszeyka Nonequilibrium Thermodynamics Laboratories, Department of Mechanical Engineering. Member AIAA.

†Professor, Michael A. Chaszeyka Nonequilibrium Thermodynamics Laboratories, Department of Mechanical Engineering. Associate Fellow AIAA.

‡Professor Emeritus, Michael A. Chaszeyka Nonequilibrium Thermodynamics Laboratories, Department of Mechanical Engineering. Fellow AIAA.

§Post-Doctoral Researcher, Department of Aerospace Engineering and Mechanics.

¶McKnight Presidential Professor and Russell J. Penrose Professor, Fellow AIAA, Department of Aerospace Engineering and Mechanics.

two-dimensional temperature and vibrational temperature fields in the flow. When the burst-mode laser is used with a high-framing-rate camera, sets of NO PLIF images can be obtained during a single run, with a frame rate of up to 500 kHz [14]. The use of the present approach is also motivated by the results of our recent measurements of vibrational level populations of nitrogen excited in the discharge in the nozzle plenum, using picosecond Coherent Anti-Stokes Raman Scattering diagnostics [11]. The use of this system makes possible vibrational temperature measurements behind the bow shock in the supersonic test section. Finally, flow modeling calculations are conducted using a three-dimensional compressible Navier–Stokes nonequilibrium flow code, fully coupled with vibrational relaxation and air chemistry models.

The first objective of the present work is to design, build, and operate a small-scale $M = 5$ test flow facility, with run time of up to a few seconds, good flow quality, ample access for optical diagnostics, and ability to generate steady-state nonequilibrium airflows. The second objective is to use high-frame-rate optical diagnostics recently developed at Ohio State University to characterize the nonequilibrium flow. Section II describes the experimental apparatus developed in the present work, a small-scale, Mach 5, non-equilibrium flow wind tunnel, with vibrational nonequlibrium sustained using a low-temperature electric discharge in the plenum, and high-frame-rate NO PLIF diagnostics. Section III.A discusses results of electric discharge characterization. Section III.B presents results of NO PLIF flow imaging and thermometry. Also, Secs. III.A and III.B compare the results of static pressure, schlieren, and NO PLIF measurements with three-dimensional computational fluid dynamics (CFD) modeling calculations. A major outcome of the present work will be development of a portable diagnostic suite capable of taking detailed flow measurements at large-scale, short-pulse hypersonic facilities, thereby enhancing considerably the range of their flow-characterization capability.

II. Experimental Apparatus and Diagnostics

A schematic of the laboratory-scale Mach 5 nonequilibrium wind tunnel is shown in Fig. 1. The wind tunnel operates using nitrogen or dry air supplied from high-pressure cylinders, at plenum pressures of $P_0 = 0.5$–1.0 atm. The tunnel is made of transparent acrylic plastic. Steady-state nonequilibrium supersonic flow in the wind tunnel is produced by sustaining a high-pressure electric discharge in the plenum. The discharge used in the present work is a combination of two fully overlapping discharges in a rectangular cross section channel 1 cm in height and 4 cm wide (see Fig. 1). The first is a transverse, nanosecond pulse discharge sustained between two plane electrodes flush mounted in the top and bottom walls of the discharge section, as shown in Fig. 1, and operated at a high pulse-repetition rate $\nu = 100$ kHz. The pulsed discharge electrodes used in the present work are square (4×4 cm) copper plates, covered with alumina ceramic dielectric plates $1/16$ in. thick, with a 10 mm gap between the surfaces of the dielectric plates. The second is transverse dc discharge sustained between two rectangular copper plate electrodes $l = 4$ cm long with a height of $h = 10$ mm, mounted in the side walls of the discharge section (see Fig. 1). The dc electrodes can be removed so that the repetitive nanosecond pulse discharge can be operated alone. Both pulsed electrodes and dc electrodes are rounded at the edges to reduce the electric field nonuniformity. The walls of the channel are covered by alumina ceramic plates attached to the walls using silicon rubber adhesive, to protect them from overheating in case of discharge instability development and arcing in the discharge section.

The main purpose of the use of two overlapping discharges is to generate stable nonequilibrium plasmas at high plenum pressures and discharge energy loading. The repetitive nanosecond pulse discharge is operated using a high peak voltage (up to 30 kV), short pulse duration (5 ns), high pulse-repetition rate, produced by a high-voltage nanosecond pulse generator (FID GmbH). The pulser is operated using an external trigger/function generator. The nanosecond pulse voltage and current are measured using short response time, capacitive voltage probe and shunt current probe, both custom designed [4]. Volume ionization in the discharge section is generated during each high-voltage nanosecond pulse, after which the voltage is turned off before ionization/heating instability has time to develop [15]. The ionizing voltage pulse is repeated before the plasma fully decays, thus generating pulse-periodic, volumetric ionization in the discharge section.

Between the ionizing pulses, energy is coupled to the flow by a dc discharge, sustained in the ionized flow when dc voltage is applied to the side wall electrodes. The dc electrodes are connected to a Glassman 5 kV, 2 A power supply, operated in a voltage-stabilized mode, in series with a 1.5 kΩ ballast resistor. The dc voltage is

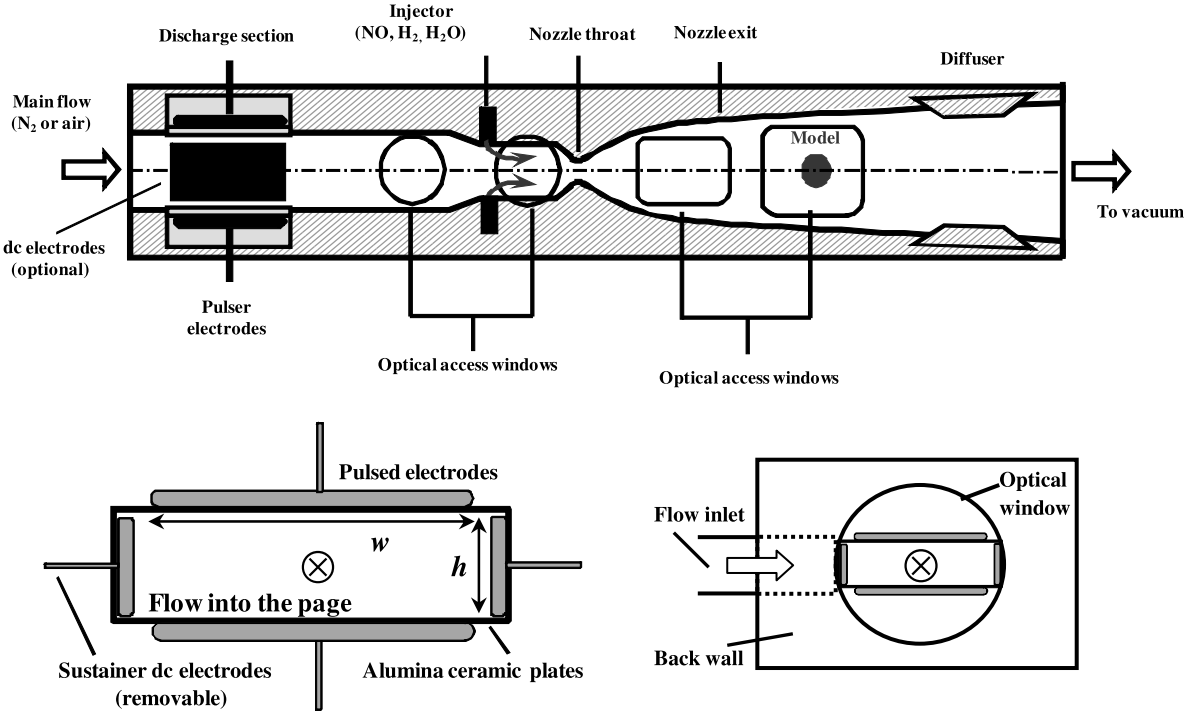

Fig. 1 Schematics of the Mach 5 wind tunnel (top), electrode arrangement in the discharge section (bottom left), and plenum flow inlet providing optical access through a window in the back wall (bottom right).

deliberately kept below breakdown threshold, typically below 4–5 kV, to preclude development of self-sustained (i.e., independent of pulsed ionization) dc discharge in a high pressure flow, which would result in instability development and arcing. If the ionizing pulses are turned off, dc voltage would not produce breakdown in the test section. The power coupled to the flow by the dc discharge is significantly higher than the repetitively pulsed discharge power. Previously, this approach has been used in our work to sustain high-power discharges in a Mach 3–4 MHD wind tunnel [8–10] and in an electrically excited gas dynamic oxygen-iodine laser [7]. In the present experiments, the repetitively pulsed discharge is operated for up to several seconds, and the dc discharge is operated for 0.5–1.0 s. The dc power supply is triggered by an externally generated rectangular shaped trigger pulse. The rising edge of the rectangular pulse also triggers the function generator, which produces a burst of trigger pulses for the high-voltage nanosecond pulse generator, at preset pulse-repetition rate and number of pulses.

The reduced electric fields in the two discharges are significantly different, $(E/N)_{\text{peak}} \sim 300$ Td in the nanosecond pulsed discharge and $E/N \sim 10$ Td in the dc discharge ($1\ \text{Td} = 10^{-17}\ \text{V}\cdot\text{cm}^2$). At these conditions, a significant fraction of input power in the pulsed discharge is spent on electronic excitation, dissociation, and ionization of nitrogen, while nearly all input power in the dc discharge (up to ~80–90% [15]) is stored in the vibrational energy mode of nitrogen, with fairly little power going to translational/rotational mode, i.e., to heat. Due to a very long N_2 vibrational relaxation time (~7 atm · s) at near-room temperature [16], this approach can create essentially vibrationally frozen nitrogen and airflows in the supersonic test section, with vibrational temperature exceeding considerably the translational/rotational mode temperature.

Optical access to the flow in the discharge section is provided through multiple optical windows, two 1.5-in.-diam BK-7 glass windows in the side walls of a separate optical diagnostics section, which can be placed between the discharge section and the nozzle (see Fig. 1), and a 2-in.-diam UV-grade fused silica window, which can be installed in the back wall of the discharge section. Recently, the optical diagnostics section has been used to measure vibrational temperature of nitrogen downstream of the discharge section, using a picosecond CARS system. The results of these measurements are discussed in detail in a separate paper [11]. The 2 in. optical access window has been used to take Intensified Charged-Coupled Device (ICCD) camera images and photographs of the discharge, as well as UV/visible emission spectra (nitrogen second positive bands) used for translational/rotational temperature inference in the discharge. The emission spectra have been taken using an optical multichannel analyzer (OMA) with a Spectra-Physics 0.25 m spectrometer with a 30 μm slit, a 1200 g/mm grating blazed at 500 nm, a PIXIS 256E 1024×256 pixel charge-coupled device (CCD) array camera, and a UV lens ($f = 100$ mm, Thorlabs), providing spectral resolution of about 0.1 nm. When the 2 in. window is used, the flow enters the discharge section at 90 deg to the wind tunnel axis, which may adversely affect the flow quality in the plenum. Therefore, in the experiments when discharge images and emission spectra are not taken, the flow enters the plenum through the back wall of the discharge section.

Downstream of the discharge section, various gases can be injected into the main flow using a choked-flow injector with 20 injection ports in the top and bottom channel walls, 1 mm in diameter each, as shown in Fig. 1. In the injector, the channel height is reduced to 5 mm to increase the flow Mach number and to improve mixing with the main flow. The flow Mach numbers in the discharge section and in the injector, estimated based on a quasi-one-dimensional isentropic flow theory, are $M \approx 0.1$–0.2 and $M \approx 0.2$, respectively. In the present work, gases injected into the main flow include oxygen, nitric oxide, hydrogen, and carbon dioxide, all diluted in nitrogen carrier. Oxygen can also be added to the main nitrogen flow excited in the discharge to create vibrationally excited synthetic airflow. Nitric oxide added to the main flow is used for NO PLIF measurements, discussed next. Finally, NO, H_2, or CO_2 injection is used to accelerate the rate of vibration–translation (V–T) or vibration–vibration (V–V) relaxation in the flow vibrationally excited in the discharge, to control vibrational energy loading of the flow in the supersonic test section.

Downstream of the injector, the flow expands through an aerodynamically contoured two-dimensional Mach 5 nozzle, with a throat height of 1.6 mm. Top and bottom walls of the supersonic test section after the nozzle exit diverge at a 1.5 deg angle each to provide boundary-layer relief. The static pressure in the supersonic section is measured using a wall pressure tap in the side wall at the end of the nozzle. A 4-cm-long, 5-mm-diam quartz cylinder model is mounted in the center of the 7-cm-long supersonic test section, i.e., 3.5 cm downstream of the end of the nozzle. The model extends wall-to-wall and is held in place using extensions placed inside circular recesses drilled in 2×2 in. UV-grade fused silica optical access windows flush mounted in the side walls of the test section. Two additional optical access windows, also 2×2 in. UV-grade fused silica, are flush mounted in the top and bottom test section walls, thus providing optical access to the supersonic test from all four directions. The windows are used for NO PLIF measurements, schlieren visualization, and emission spectroscopy measurements.

Downstream of the test section, a supersonic diffuser with a 5 deg step angle is used to improve pressure recovery before the flow exits into an 8-in.-diam vacuum pipe, connected to a 110 ft^3 vacuum tank and a 200 cfm vacuum pump. At the baseline conditions, plenum pressure of $P_0 = 370 \pm 0.05$ torr, the test section static pressure is $P = 1.2 \pm 0.05$ torr, corresponding to the Mach number of $M = 4.55 \pm 0.03$. During the experiment, both the main flow through the discharge and the injection flows are controlled using solenoid valves. The main flow rate is calculated using a choked-flow equation, based on the plenum pressure and the nozzle throat area. Injection flow rates have been both measured using a mass flow controller. At the baseline conditions, nitrogen at $P_0 = 0.5$–1.0 atm, the mass flow rate through the tunnel is 7.5–15.0 g/s and the steady-state run time at the constant static pressure in the supersonic test section is 5–10 s. The runs can be repeated every few minutes.

The shock wave standing in front of the cylinder model in the supersonic test section is visualized by schlieren diagnostics. The schlieren system uses a high-power green LED with a thermoelectric cooler as a continuous light source and a complementary metal–oxide–semiconductor camera operated in video mode (exposure time 1.5 ms, frame rate 4 to 8 frames per second). Taking schlieren images is not synchronized with the discharge operation, but correct timing is controlled by partially overlapping the plasma image with the schlieren image on the camera. Optical access on all four sides of the test section enables taking schlieren images of the shock from two different directions, both parallel and perpendicular to the cylinder model axis (side view and top view).

Flowfield in the supersonic test section is visualized by high-frame-rate NO PLIF, using a custom design, tunable burst-mode laser described in detail in [12,13]. The laser is capable of generating bursts of 10 to 20 pulses at the fundamental frequency of 1064 nm, at a high pulse-repetition rate, 10–500 kHz, burst repetition rate of 1 Hz, and pulse energy of up to 100 mJ/pulse. The laser is tunable in a wide range of wavelengths, using nonlinear wave mixing and a custom-design optical parametric oscillator. For high-frame-rate NO PLIF imaging, the laser-generated bursts of 10–20 pulses in the vicinity of 226 nm, at a pulse-repetition rate of 10–20 kHz (0.05–0.1 ms burst duration) and a pulse energy of ~0.3 mJ/pulse [14]. The laser was operated both in a broadband mode and in the injection-seeded mode, to produce narrow linewidth (~0.01 cm^{-1}) tunable output, providing access to $\text{NO}(X^2\Pi_{1/2}, v' \rightarrow A^2\Sigma, v'')$ absorption transitions. Laser output wavelength was measured with a wavemeter (HighFinesse GmbH, model WS6). Nitric oxide was seeded into the flow through the injector in the subsonic part of the wind tunnel, as discussed previously, or through the short cylinder model in the supersonic test section, using a 20%NO–80%N_2 mixture. Baseline NO mole fraction in the main flow with subsonic injection was 0.3%. NO PLIF measurements have also been conducted in unseeded airflows using nitric oxide generated in the electric discharge in the plenum.

Injection-seeded (single-line) laser operation was used to pump NO on two different rotational lines of the $v' = 0 \rightarrow v'' = 0$ band,

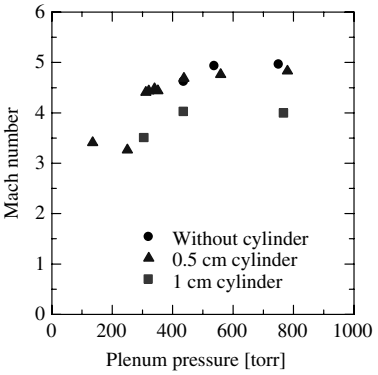

Fig. 2 Test section Mach number vs. plenum pressure, inferred from the static pressure measured at the end of the nozzle. At $P_0 = 760 \pm 0.05$ torr, baseline test section static pressure is $P = 1.5 \pm 0.05$ torr.

$Q_1 + P_{21}$ ($J = 5.5$) line at 226.17 nm and $Q_1 + P_{21}$ ($J = 16.5$) line at 225.88 nm, to measure the rotational temperature in the supersonic test section, as well as on a single rotational line of the $v' = 1 \rightarrow v'' = 1$ band, $Q_1 + P_{21}$ ($J = 3.5$) at 223.83 nm, to measure NO vibrational temperature. The laser sheet, approximately 2.5 cm wide, was directed through the supersonic test section vertically, using optical access windows in the top and bottom walls. NO fluorescence was collected at 90 deg through the side window and detected by a PI-MAX UV-I CCD camera (Princeton Instruments) with a UV lens ($f = 100$ mm, Thorlabs). The camera gate was set at 1 ms to accumulate fluorescence signal after excitation by 10 pump-laser pulses, with the laser operating at a 10 kHz pulse-repetition rate. To monitor the intensity distribution across the laser sheet, approximately 5% of the incident sheet was reflected off a glass plate placed 2 cm above the wind tunnel and directed into a cell filled with a Rhodamine 640 dye diluted in methanol. The fluorescence from the dye in the cell, between 570 to 600 nm, was recorded using a PIXIS 256E 1024×256 pixel CCD array camera (Princeton Instruments), thus yielding the laser sheet intensity distribution. The NO PLIF signal distribution was normalized on the laser sheet intensity distribution during postprocessing of the experimental data.

Emission spectra from the flowing afterglow in the supersonic test section have been taken using the same OMA system as discussed previously. Afterglow images were taken using either the PI-MAX ICCD camera or the Andor iStar ICCD camera.

III. Results and Discussion

A. Flow and Discharge Characterization

Figure 2 plots the Mach number in the supersonic test section versus the plenum pressure, inferred from wall static pressure measurements at the end of the Mach 5 nozzle. The static pressure was measured in the cold nitrogen flow (without the discharge in the plenum) for three different sets of conditions: 1) without a cylinder model in the test section, 2) with a 5-mm-diam cylinder model, and 3) with a 10-mm-diam model. It can be seen that, as the plenum pressure is increased, the Mach number measured without the model in the test section approaches the design Mach 5 value, $M = 4.5$–5.0 at $P_0 = 380$–760 torr. One can also see that installing the 5-mm-diam model has a fairly minor effect on the static pressure and the Mach number, $M = 4.5$–4.8 at $P_0 = 380$–760 torr. With the 10-mm-diam model in the test section, the Mach number decreases significantly, to $M = 4.0$ at $P_0 = 440$–760 torr. As the cylinder model diameter is increased, the static pressure rise and the apparent Mach number reduction are most likely due to boundary-layer buildup on the plane side walls of the tunnel, affected by the secondary cross flow [10], and its interaction with the model, which produces significant flow blockage.

These results are consistent with the predictions of CFD calculations using a hybrid, implicit unstructured fully coupled finite-volume solver (US3D) [17,18] that solves the compressible Navier–Stokes equations to compute the flowfield. The inviscid fluxes are calculated using a low-dissipation version of Steger–Warming flux vector splitting [19]. This uses exact linearization of the fluxes and upwind biasing using the signs of the eigenvalues. Second- or third-order accuracy is achieved by using an upwind biased monotone upstream-centered scheme for conservation laws approach. The viscous fluxes are evaluated using weighted least-squares fits with the deferred correction approach [20]. Time integration is performed implicitly. A parallel-line relaxation procedure [21] is used in areas where grids are severely stretched and lines of grids can be assembled (near the surfaces). In regions where such construction cannot be achieved, a full-matrix point relaxation [22] method is adopted. A subsonic inflow boundary condition is used for the nozzle [23]. The simulations were carried out using an unstructured grid with 7.1 million grid points with cells clustered close to the nozzle walls, shown in Fig. 3. The grid also has higher density close to the cylinder model for better resolution of flow features. Although US3D code has a capability to model compressible flows with vibrational and chemical nonequilibrium, in the present work only equilibrium flows have been modeled. Figure 4 shows the code predictions for nitrogen flow at $P_0 =$ 380 torr and $T_0 = 300$ K. The predicted side wall static pressure 4 cm upstream of the cylinder model is 1.08 torr, which is close to the measured static pressure at this location, 1.2 torr. It can be seen that the Mach number upstream of the 5-mm-diam cylinder model is about $M = 4.5$, in good agreement with the Mach number inferred from the static pressure measurement. One can also see "bulges" developing in the side-wall boundary layers due to the secondary cross flow. However, approximately 50% of the test section width upstream of the cylinder is occupied with an "inviscid core" flow with $M = 4.5$.

Figure 5 show ICCD camera images of a repetitive nanosecond pulse discharge in nitrogen at a pressure of $P_0 = 350$ torr and a pulse-repetition rate of $\nu = 100$ kHz. These images were taken through the 2-in.-diam window in the back wall of the discharge section, as discussed in Sec. II, for a 1 cm gap between the pulsed electrodes, pulsed electrodes width of $w = 3$ cm, and with the dc electrodes removed from the discharge section. The images shown in Fig. 5 are for pulses 100 and 1000 during the discharge pulse burst, with the camera gate, 5 μs long, including one discharge pulse. The plasma emission decay time is also approximately 5 μs; no change in emission intensity was detected for longer camera gates. From Fig. 5,

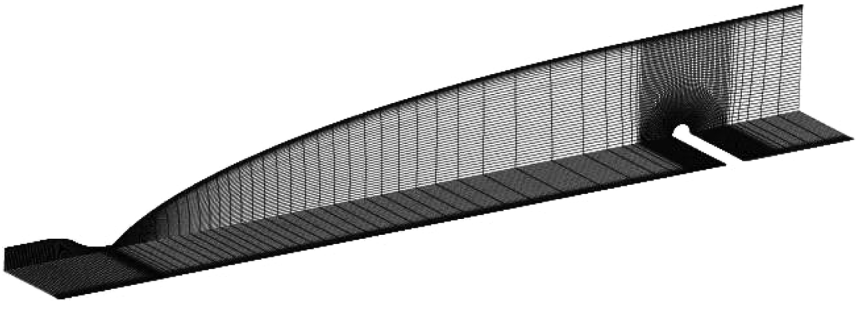

Fig. 3 Grid used for simulating the flow in the Mach 5 wind tunnel, including the cylinder model in the supersonic section. The grid is coarsened by a factor of 2 for clarity.

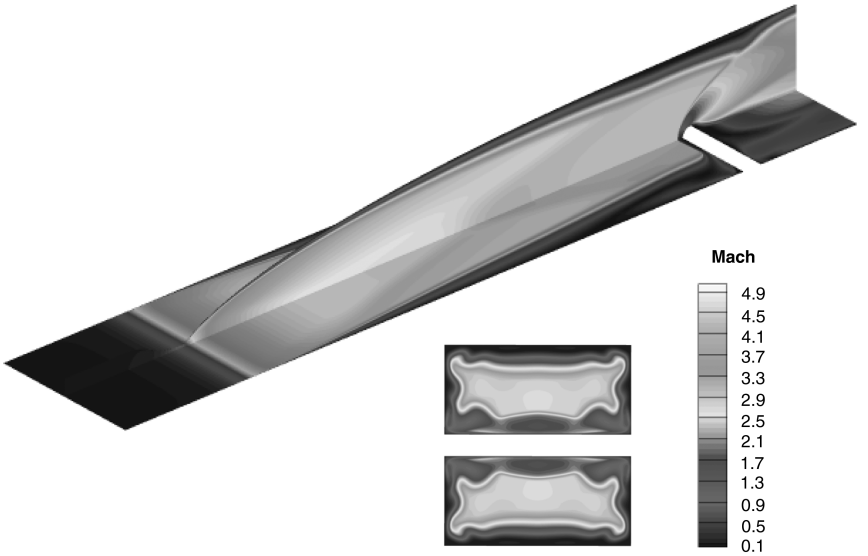

Fig. 4 Mach number distributions in the entire wind tunnel (top) and in the flow cross section through the cylinder model axis (bottom), predicted by a three-dimensional Navier–Stokes code.

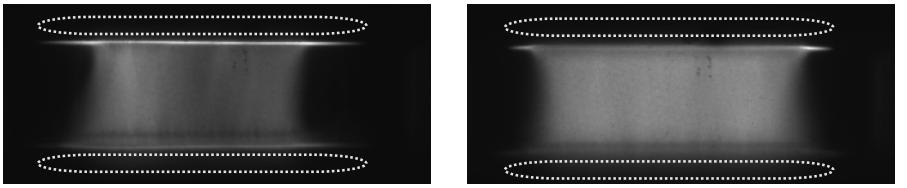

Fig. 5 ICCD camera images of a nanosecond pulsed discharge in nitrogen at $P_0 = 350$ torr. Pulse-repetition rate $\nu = 100$ kHz. Pulses 100 (left) and 1000 (right).

it can be seen that, during pulse 100, uniform plasma occupies approximately $\frac{3}{4}$ of the pulsed electrodes width and, during pulse 1000 (i.e., 10 ms after beginning of the burst), the plasma fills nearly the entire discharge volume.

Figure 6 shows typical pulse voltage and current traces (top), as well as instantaneous power and coupled pulse energy traces (bottom), measured in a repetitively pulsed discharge in nitrogen at $P_0 = 350$ torr and $\nu = 100$ kHz, without dc electrodes present in the test section. The waveforms shown are for a pulse generated 0.1 s after the beginning of the pulse burst (i.e., for pulse 10,000). At these conditions, the pulse peak voltage and current are 25 kV and 64 A, respectively, with the voltage pulse FWHM of 5 ns, and the coupled pulse energy of 5.4 mJ/pulse (time-averaged pulsed discharge power 540 W). In Fig. 6, several successive pulse reflections can be identified, separated by approximately 40 ns, which couple additional energy to the plasma.

The coupled pulse energy dependence on the discharge pressure (both for the incident pulse only and after several pulse reflections) is shown in Fig. 7. Also plotted in Fig. 7 is the ratio of peak pulse voltage and peak current, which can be used as an estimate of plasma impedance. It can be seen that the estimated impedance increases with the discharge pressure. At $P_0 = 350$–400 torr, the plasma impedance becomes close to the total impedance of the four-channel coaxial transmission line between the pulsed power supply and the pulsed discharge electrodes, $Z = 400\ \Omega$. As can be seen from Fig. 7, at these conditions the energy coupled to the plasma by the incident pulse appears to reach a broad maximum, 4.5 mJ/pulse. Energy coupled to the plasma during the incident discharge pulse decreases at higher and especially at low pressures. However, when the energy coupled to the plasma by multiple reflected pulses is taken into

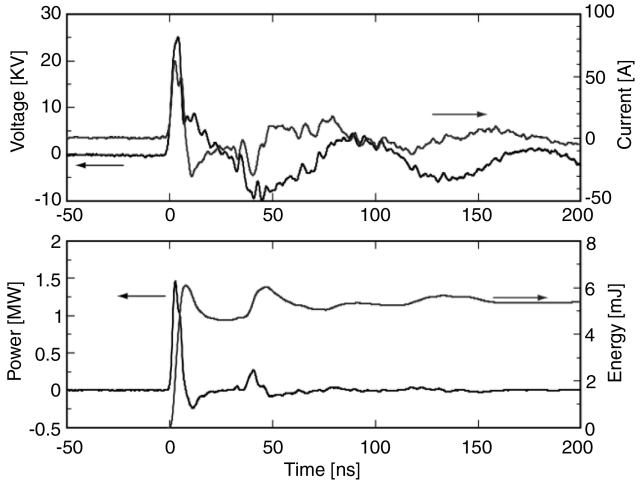

Fig. 6 Pulse voltage and current waveforms (top), instantaneous power and coupled energy (bottom) in nitrogen at $P_0 = 350$ torr and $\nu = 100$ kHz (pulse 10,000).

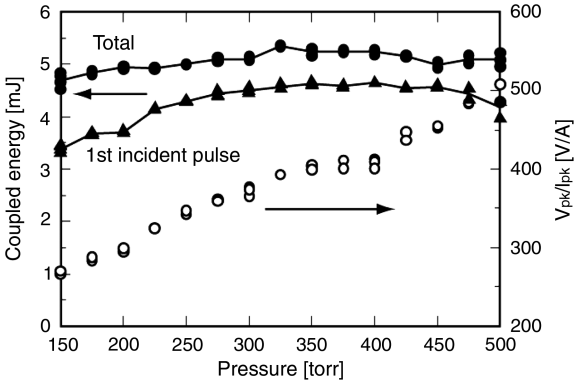

Fig. 7 Coupled pulse energy and estimated plasma impedance vs. discharge pressure. Nitrogen, $\nu = 100$ kHz, pulse 10,000.

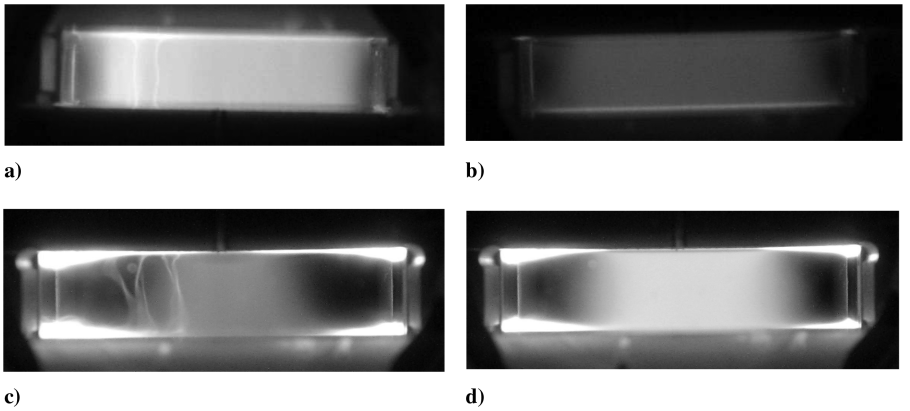

Fig. 8 Photographs of the pulsed and pulsed/dc discharges. a) $P_0 = 300$ torr, no dc electrodes; b) $P_0 = 650$ torr, no dc electrodes; c) $P_0 = 350$ torr, $U_{PS} = 0$ kV; d) $P_0 = 350$ torr, $U_{PS} = 2.0$ kV.

account, the total pulse energy remains nearly constant at approximately 5 mJ/pulse (see Fig. 7).

Figure 8 shows photographs of the repetitive nanosecond pulse discharge (a and b) and of the overlapped repetitively pulsed/dc discharges (c and d) in nitrogen at different plenum pressures. These photos were taken through the 2-in.-diam window in the backplate of the discharge section, as discussed in Sec. II. In Figs. 8a and 8b, the nanosecond pulse discharge is operating at the pulse-repetition rate of $\nu = 100$ kHz, using square 4×4 cm pulsed electrodes, and with the dc electrodes removed from the discharge section. It can be seen that the discharge produces diffuse and uniform plasma, filling nearly the entire discharge section. At fairly low plenum pressures, $P_0 = 300$ torr, arc filaments sometimes form in the plasma (e.g., see Fig. 8a). However, the filaments disappear as the plenum pressure is increased to $P_0 = 650$ torr (see Fig. 8b).

Adding the dc electrodes to the discharge section, even without applying voltage to them, changes the plasma behavior dramatically (see Fig. 8c). Qualitatively, placing the copper plate dc electrodes along the side walls concentrates the electric field and provides an additional current path between the pulsed electrodes via the dc electrodes. Therefore, although some of the diffuse plasma remains in the center of the discharge section, away from the side walls, there are also much brighter plasma regions formed in the four corners, near the rounded edges of the dc electrode plates, with a few filaments extending between the pulsed electrodes (see Fig. 8c). Applying the dc voltage to the electrodes and increasing it removes the filaments and results in significant growth of the diffuse plasma volume in the center of the discharge section (see Fig. 8d). However, the presence of additional current paths in the corners creates a significant uncertainty in estimating the power loading in the diffuse discharge in the center. A substantial fraction of the discharge input power may be dissipated in the corner regions of the discharge section, thereby reducing the energy loading in the center and also adversely affecting the flow quality. In Fig. 6, the dc voltage applied by the power supply is $U_{PS} = 2$ kV. The actual voltage between the dc electrodes is significantly lower because of the voltage drop on a 1.5 kΩ ballast resistor connected in series with the dc discharge gap.

Figure 9 shows typical dc discharge current traces measured at the same flow and pulsed discharge conditions as in Figs. 8c and 8d, for different dc power supply voltages, $U_{PS} = 1$–4 kV. It can be seen that the current increases sharply after every nanosecond discharge pulse (generated every 10 μs), which is the sole source of ionization in the non-self-sustained dc discharge outside the cathode layer [15,24]. Between the pulses, the current gradually decays due to electron–ion recombination. Figure 10 plots the current voltage characteristic (time-averaged dc discharge current, $\langle I \rangle$, versus time-averaged voltage between the dc electrodes, $\langle U \rangle = U_{PS} - \langle I \rangle R$) at the conditions of Fig. 9. As expected, the current exhibits a linear rise typical for non-self-sustained discharges [8], indicating that no additional ionization source (expect for ionization by the nanosecond pulse discharge) exists in the entire range of dc voltages used. An x-axis intercept of a linear fit to the current voltage characteristic of Fig. 10, approximately 300 V, gives the voltage fall across the self-sustained cathode layer of the dc discharge. Basically, the non-self-sustained dc discharge current remains near zero until the cathode layer becomes self-sustained [15,24].

Rotational–translational temperature in the discharge was inferred from the N_2 second positive band emission spectra, taken through the 2-in.-diam window in the backplate of the discharge section. To isolate emission from the diffuse plasma in the center of the discharge section (see Figs. 8c and 8d), the emission was apertured using an iris diaphragm with a 5-mm-diam opening. Figure 11 shows a typical emission spectrum ($0 \rightarrow 2$ band) along with the best fit synthetic spectrum, calculated using nitrogen molecular constants [25], rotational line intensities [26], and the experimentally measured slit function of the spectrometer. Figure 12 shows temperatures inferred from the synthetic spectra such as shown in Fig. 11, plotted versus dc voltage between the electrodes. The uncertainty of the temperature

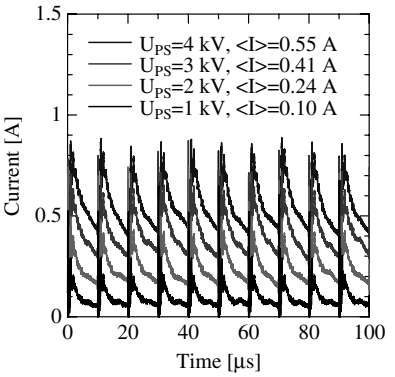

Fig. 9 The dc sustainer current traces for different dc power supply voltages (indicated in the plot). Nitrogen, $P_0 = 350$ torr, $\nu = 100$ kHz.

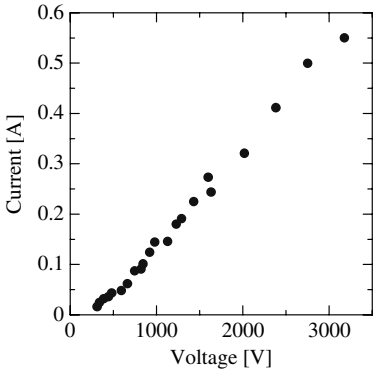

Fig. 10 Current voltage characteristic (time-averaged current vs time-averaged voltage between dc electrodes) at the conditions of Fig. 9.

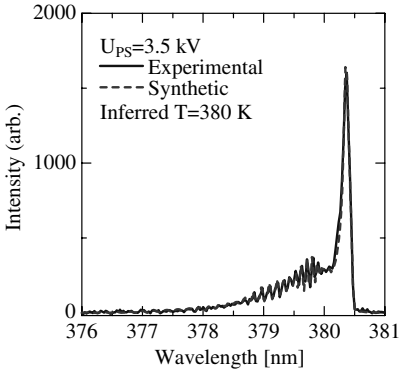

Fig. 11 Nitrogen second positive emission spectrum ($0 \rightarrow 2$ band) from the pulser–sustainer discharge in the nozzle plenum and best fit synthetic spectrum. Nitrogen, $P_0 = 350$ torr, dc power supply voltage $U_{PS} = 3.5$ kV.

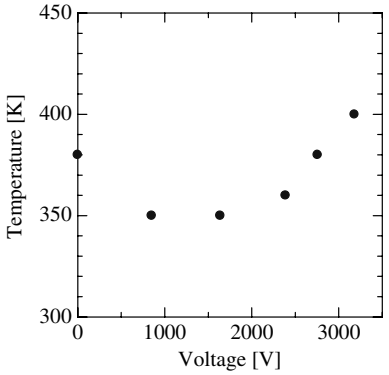

Fig. 12 Temperature in the discharge section (stagnation temperature) vs voltage between dc electrodes at the conditions of Figs. 9 and 10.

inference is approximately ±25 K. As can be seen, at high dc voltages, $\langle U \rangle = 2.3$–3.2 kV, the temperature is increasing, reaching $T_0 = 400$ K at $\langle U \rangle = 3.2$ kV. However, the temperature does not approach room temperature at low dc voltages, below 1.7 kV, and at $U = 0$ the inferred temperature is actually higher than at nonzero dc voltage. This occurs most likely due to emission from higher-temperature regions in the corners of the discharge section (see Figs. 8c and 8d), collected by the OMA spectrometer in spite of using the iris aperture.

Figure 13 plots the time-averaged dc discharge power (i.e., the product of the time averaged current and voltage shown in Fig. 10) versus the time-averaged dc voltage between the electrodes, as well as the estimated power stored in the vibrational mode of nitrogen. The discharge power plotted in Fig. 13 represents the total power coupled both to the diffuse plasma in the center and to the regions in the corners of the discharge sections (see Fig. 8d). The fraction of the discharge power loaded into N_2 vibrational energy mode by electron impact in nitrogen was predicted by solving the two-term Boltzmann equation for the plasma electrons [27] with the cross sections taken from [28]. The reduced electric field, used as an input parameter by the Boltzmann solver, is calculated from the time-averaged dc voltage between the electrodes, $\langle E/N \rangle_{DC} = 2.5$–$7.5$ Td. According to the Boltzmann-solver prediction, 50 to 80% of the input dc discharge power at these conditions is spent on nitrogen vibrational excitation. From Fig. 13, it can be seen that, at the highest dc voltage between the electrodes, $\langle U \rangle = 3.2$ kV (at $U_{PS} = 4.0$ kV and $\langle I \rangle = 0.55$ A), the total dc discharge power is 1.8 kW, with estimated 1.4 kW stored in the nitrogen vibrational mode. Note, however, that this prediction represents an upper bound because a significant fraction of the dc discharge power may be dissipated in the corners of the discharge section (see Fig. 8d), thus considerably reducing the vibrational energy loading in the bulk of the flow. Comparing the repetitive nanosecond pulse discharge power (≈0.5 kW, see Fig. 7) and the dc discharge power demonstrates that energy addition by the pulsed discharge is a relatively small fraction of the total energy loading (approximately 20% at $\langle U \rangle = 3.2$ kV).

The upper-bound vibrational energy loading per molecule and nitrogen vibrational temperature, based on the predicted power loading into the nitrogen vibrational energy mode (see Fig. 13), are plotted in Fig. 14. One can see that, at the highest dc voltage between the electrodes, $\langle U \rangle = 3.2$ kV, the estimated vibrational energy loading is approximately $\varepsilon_{vib} \approx 60$ meV/molecule, which corresponds to the vibrational temperature of $T_v(N_2) \approx 1900$ K. This is consistent with our recent measurements of nitrogen vibrational temperature using picosecond CARS diagnostics, $T_v(N_2) = 1650$ K at $\varepsilon_{vib} = 67$ meV/molecule and $T_v(N_2) = 1950$ K at $\varepsilon_{vib} = 82$ meV/molecule [11]. Somewhat lower vibrational temperature measured by CARS, compared to the model prediction, is most likely due to higher discharge energy loading in the corners of the discharge region (see Fig. 8d) and consequently lower energy loading on the flow centerline. Note that, if all energy coupled to the flow by the pulser–sustainer discharge is thermalized, the flow temperature would increase significantly, by approximately $\Delta T \approx 300$ K at the pulsed discharge power of 0.5 kW, sustainer discharge power of 1.8 kW, and plenum pressure of $P_0 = 350$ torr. This temperature rise is significantly higher than measured by emission spectroscopy in the discharge section, up to $\Delta T \approx 100$ K, indicating significant energy storage in the vibrational energy mode of nitrogen.

Figure 15, taken from our recent paper discussing nitrogen vibrational temperature measurements using a picosecond CARS system [11], illustrates the effect of injecting various gases downstream of the discharge section (O_2, H_2, NO, and CO_2) into the nitrogen flow vibrationally excited in the pulser–sustainer discharge (see Fig. 1). These results illustrate that vibrational disequilibrium of the flow in the Mach 5 test section can be varied over a wide range by injecting "relaxer" species into the plenum, thus controlling the rate of vibrational relaxation of nitrogen by V–T and V–V processes. Detailed discussion of vibrational and rotational temperature

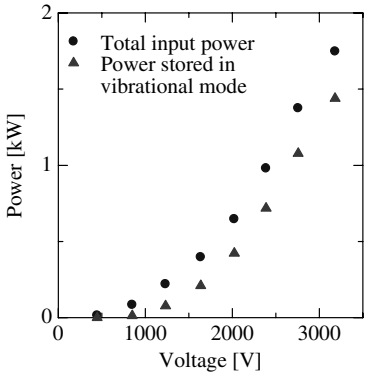

Fig. 13 Time-averaged dc discharge power vs time-averaged voltage between dc electrodes and estimated power loading into nitrogen vibrational mode at the conditions of Figs. 9 and 10.

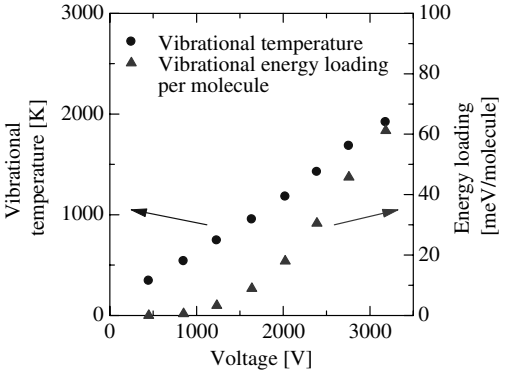

Fig. 14 Upper-bound estimate vibrational energy loading per molecule and nitrogen vibrational temperature at the conditions of Figs. 9 and 10.

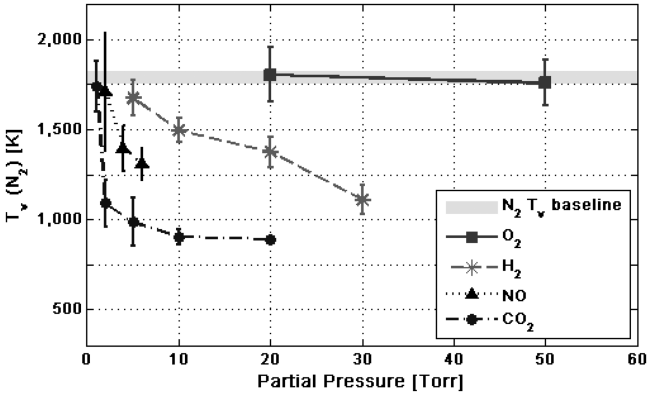

Fig. 15 Effect of injecting varies gases into nitrogen flow excited in the pulser–sustainer discharge on $T_v(N_2)$ [11]. $P_0 = 300$ torr, $\nu = 100$ kHz, $U_{PS} = 5$ kV, with a modified discharge section.

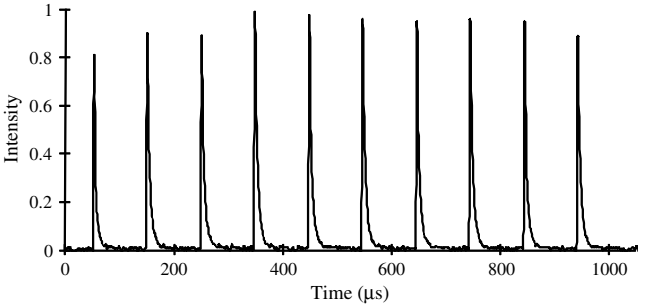

Fig. 17 Typical burst-mode laser output at 226 nm, at a pulse-repetition rate of 10 kHz (10 pulses per burst). Pulse energy 0.3 mJ/pulse.

measurements using picosecond CARS diagnostics can be found in [11].

B. NO PLIF Measurements

Figure 16 shows schlieren images of a bow shock in front of a 5-mm-diam cylinder model in the supersonic test section (top view and side view). These images were taken in cold nitrogen flow at $P_0 = 350$ torr, without the discharge in the plenum. At these conditions, the shock standoff distance is 1.2 ± 0.05 mm, with the shock extending across the flow over approximately 20 mm, i.e., over about half of the test section width. Figure 16 also shows synthetic schlieren bow shock images (contour plots of density gradient) predicted by the three-dimensional compressible Navier–Stokes code. It can be seen that the shock standoff distance and the spanwise extent predicted by the code are in good agreement with the experiment.

Figure 17 shows typical burst-mode laser output at 226 nm, at a pulse-repetition rate of 10 kHz (10 pulses per burst, burst duration 1 ms) and a pulse energy of 0.3 mJ/pulse, illustrating good shot-to-shot pulse energy reproducibility as well as the capability of taking multiple NO PLIF images in a single run using the present diagnostics. As discussed in Sec. II, in the present experiments the burst-mode laser has been used for NO PLIF flow visualization. During most of NO PLIF measurements, the flow was seeded with nitric oxide at a ~0.1–1.0% level, using subsonic injection of a 20% NO–N_2 mixture into the main flow downstream of the discharge section (see Fig. 1).

Figure 18 compares four NO PLIF images of Mach 5 flows over a 5-mm-diam cylinder model. Figure 18a shows an image of NO-seeded nitrogen flow, at $P_0 = 350$ torr and without the discharge sustained in the plenum. To obtain this image, the laser was operated in a broadband mode, at a pulse-repetition rate of 20 kHz, 10 pulses/burst (0.5 ms burst duration), and burst repetition rate of 1 Hz. During broadband operation, absorption by NO occurs on multiple rotational transitions of the NO($X, v'' = 0 \rightarrow A, v' = 0$) absorption band. The fluorescence signal in Fig. 18a was integrated over 10 laser pulses (i.e., over 0.5 ms), and the NO mole fraction in the flow was 1%. The bow shock in the flow over the cylinder model and the wake behind the cylinder are clearly visible. The wake region appears dark because of a low density in the wake region, compared to the density elsewhere behind the bow shock (by approximately a factor of 50 according to the CFD code prediction). Note that the laser beam is transmitted through the transparent cylinder model, which is made of quartz, and therefore the fluorescence signal is also detected below the cylinder (see Fig. 18a). The bright spot immediately below the model occurs due to lensing of the laser beam by the cylinder and subsequent strong fluorescence from laser-excited NO molecules at the focal point. A single laser pulse broadband NO PLIF image obtained at the same flow conditions, with 3% NO mole fraction in the flow, is shown in Fig. 18b, demonstrating feasibility of taking multiple (up to ~10) images during the same run, if a MHz-rate-framing camera is used together with the burst-mode laser.

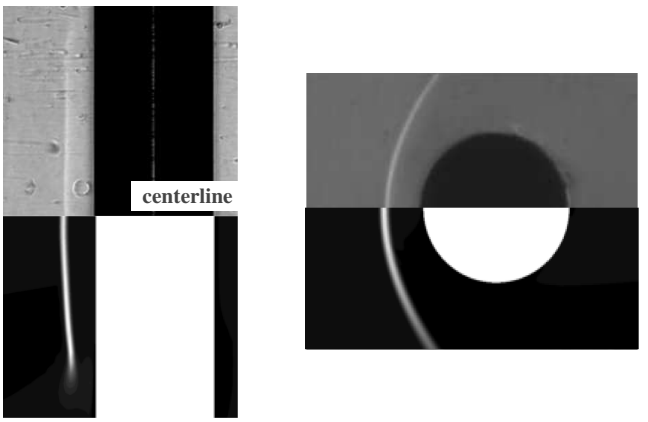

Fig. 16 Comparison of experimental (top) and CFD (bottom) schlieren images (top view and side view). Nitrogen, $P_0 = 350$ torr, cold flow (no plasma). Shock stand-off distance 1.2 mm.

Figure 18c demonstrates feasibility of the use of NO PLIF images for measurements of two-dimensional rotational/translational temperature distributions in supersonic flows, showing a single-line NO PLIF image of a nitrogen flow behind the bow shock, again at $P_0 = 350$ torr and without the discharge sustained in the plenum. To obtain this image, the laser was operated in the injection-seeded (single-line) mode, on a pump transition NO($X, 0 \rightarrow A, 0$), $R11 + R21(J = 11.5)$, at the same pulse-repetition rate, number of pulses in the burst, and burst repetition rate as in Figs. 18a and 18b. The image in Fig. 18c is integrated over 40 pulses (i.e., over four 10-pulse bursts), with NO mole fraction in the flow of 0.3%. In principle, the rotational temperature distribution behind the shock can be obtained from the intensity ratio of two single-line images such as shown in Fig. 18c. However, accurate quantitative temperature measurements using single-line NO PLIF images are quite challenging. First, because the laser can only be operated on a single line during the run, a pair of PLIF images for temperature inference needs to be obtained in two different runs. Second, in both cases the laser needs to be tuned accurately to NO absorption line centers. Third, laser pulse energies and laser beam intensity distributions on two different rotational transitions can be different and need to be monitored during the runs to take them into account during data reduction. Finally, the NO mole fraction in the flow needs to be sufficiently low to make sure that the flow remains optically thin.

Figure 18d demonstrates NO PLIF flow visualization in unseeded airflow. This image was taken in dry air at $P_0 = 350$ torr, excited by a repetitively pulsed nanosecond discharge in the plenum ($\nu =$ 100 kHz), without the dc discharge. The laser was operated in the injection-seeded mode, at the same pulse-repetition rate, number of pulses in the burst, and burst repetition rate as in Figs. 18a–18c. The image was integrated over 50 pulses (i.e., five 10-pulse bursts). In our previous experiments [29], the number density of nitric oxide generated in a single-pulse nanosecond discharge in dry air at $P = 60$ torr, ≈4 ppm/pulse, was measured using calibrated NO

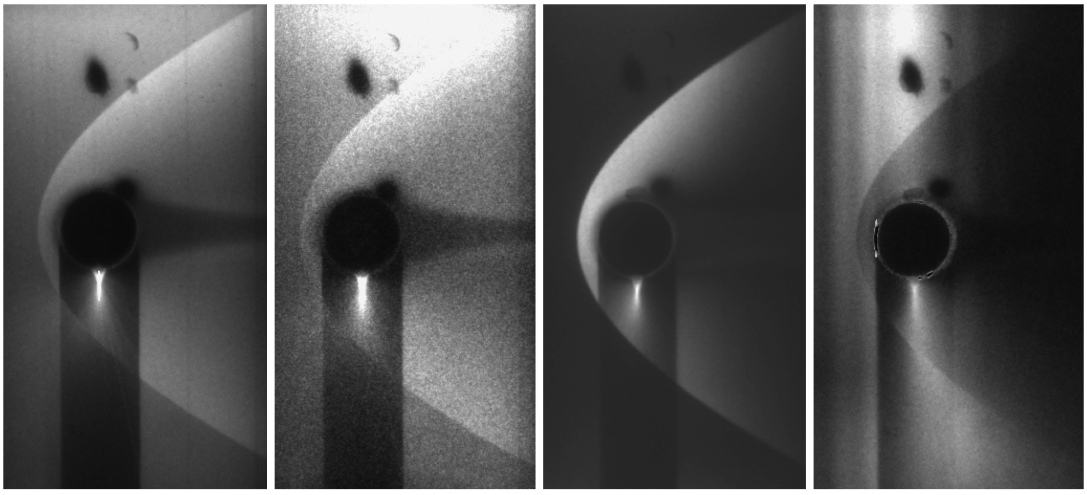

a) b) c) d)

Fig. 18 NO PLIF images taken with; a) broadband, 10-pulse integration, nitrogen, no discharge; b) broadband, single-pulse, nitrogen, no discharge; c) single-line, nitrogen, no discharge; d) single-line, unseeded air with pulsed discharge.

PLIF. At the conditions of the present experiments, the NO mole fraction generated in the repetitively pulsed nanosecond discharge in the plenum (over ~100 pulses during the ~1 ms residence time of the flow in the discharge), predicted by the kinetic model [29] is approximately 500 ppm. From Fig. 18d, it is obvious that the amount of NO generated in the discharge is sufficient to visualize the bow shock flow over the cylinder model, in spite of a much faster quenching of NO(A) state in air compared to nitrogen, by three orders of magnitude [29]. One qualitative feature apparent from Fig. 18d is unexpected and remains not fully understood. In the PLIF image, the NO fluorescence intensity behind the bow shock actually decreases, instead of increasing approximately proportional to the flow number density, as occurs in Figs. 18a–18c. This behavior suggests that the NO PLIF signal may be affected by kinetic processes in the nonequilibrium flow downstream of the discharge, such as NO vibrational relaxation.

Figure 19 compares NO PLIF images of Figs. 18a and 18c with Mach number distribution (left) and the temperature distribution (right) predicted by the three-dimensional compressible Navier–Stokes flow code for nitrogen at $P_0 = 350$ torr (without the discharge in plenum). It can be seen that the code predictions are in good qualitative agreement with the flow visualization images. In particular, bow shock shape and standoff distance as well as the size of the wake behind the model are reproduced well by the flow code.

Figure 20 compares two NO PLIF images of NO-seeded nitrogen flow in the supersonic test section (NO mole fraction of 0.3%) at $P_0 = 370$ torr, without the discharge in the plenum. To obtain these images, the laser was operated in the injection-seeded (single-line) mode, at a pulse-repetition rate of 10 kHz, 10 pulses/burst, and burst repetition rate of 1 Hz. The left image was taken by exciting the NO ground state molecule on a rotational line with a low J value, $\mathrm{NO}(X, v' = 0 \rightarrow A, v'' = 0), Q_{11} + P_{21}\ (J = 5.5)$. The image on the right is taken with the laser operating on a rotational line with a high J value, $\mathrm{NO}(X, v' = 0 \rightarrow A, v'' = 0),\ Q_{11} + P_{21}\ \ (J = 16.5)$. Both images are accumulated over 10 laser pulses and are shown on the same intensity scale. In the $J = 5.5$ image on the left, the bow shock front in the flow ahead of the cylinder model and the wake structure behind the cylinder are clearly visualized. In the $J = 16.5$ image on the right, the fluorescence intensity is significantly lower due to a lower Boltzmann factor, as expected. The $J = 16.5$ fluorescence intensity near the stagnation point is about a factor of two lower compared to the $J = 5.5$ fluorescence intensity in the same region.

Figure 21 shows two-dimensional rotational temperature distributions in a nitrogen flow behind the bow shock at $P_0 =$

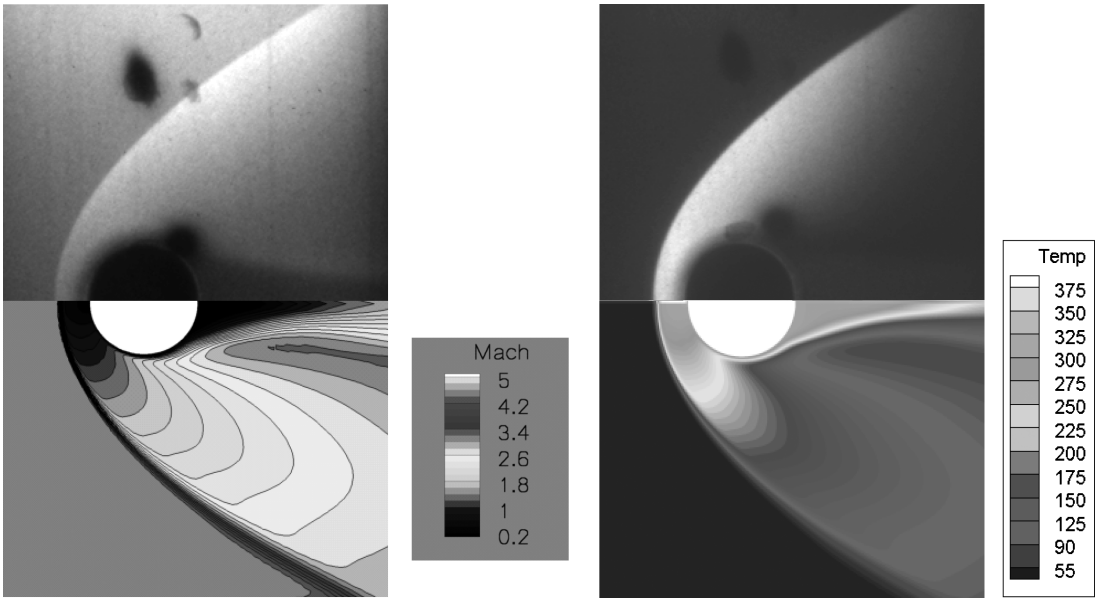

Fig. 19 Comparison of NO PLIF images with CFD predictions. Left: Fig. 18a and Mach number distribution. Right: Fig. 18b and temperature field. Nitrogen, $P_0 = 350$ torr, no discharge.

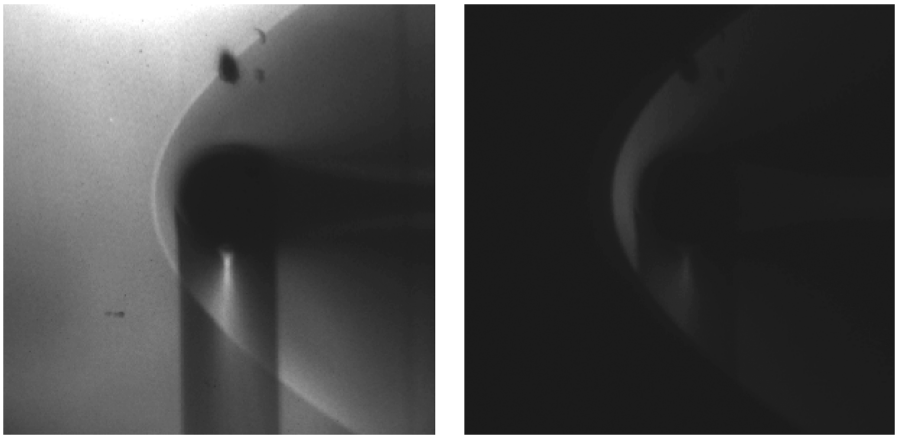

Fig. 20 NO PLIF images for single-line pumping on $J = 5.5$ (left) and $J = 16.5$ (right). Nitrogen, $P_0 = 370$ torr, NO mole fraction 0.3%, no discharge. Laser pulse-repetition rate 10 kHz, images accumulated over 10 laser pulses.

370 torr, inferred from the intensity ratio of two single-line PLIF images, $J = 5.5$ and $J = 16.5$, such as shown in Fig. 20. The temperature distributions are shown for two cases, cold flow (no discharge in the plenum) and pulsed/dc discharge excited flow ($\nu = 100$ kHz, $U_{PS} = 4.5$ kV). To calculate the temperature distributions, intensity ratios were calculated and rotational temperature was inferred for five pairs of NO PLIF images, averaged over 10 laser pulses each (both for $J = 5.5$ and for $J = 16.5$). For each image, apparent fluorescence intensity distribution was corrected by normalizing it on the intensity distribution across the laser sheet, measured at the same time (see Sec. II). Note that laser sheet intensity distributions are different when the laser is operating on $J = 5.5$ and on $J = 16.5$ lines and may vary pulse-to-pulse. In the present work, the laser intensity attenuation along the optical path, apparent in the PLIF images in Fig. 20, has not been taken into account. During calibration in a room-temperature, stagnant N_2–NO mixture, at the number density close to the number density in the flow behind the bow shock ($P = 30$ torr), fluorescence intensity attenuation for $J = 5.5$ and $J = 16.5$ lines was measured to be 19%/cm and 23%/cm, respectively. This difference would produce a temperature uncertainty of approximately 20 K over the signal collection region of 2 cm. The calculated laser beam absorption coefficients in the freestream are low, ~2%/cm. Therefore the effect of laser sheet intensity change along the optical path was neglected. The average temperature distribution and the standard deviation were calculated using the temperature distributions obtained from individual image pairs. This procedure helps reduce the effect of laser pulse energy variation pulse-to-pulse.

From Fig. 21, it can be seen that temperatures inferred at the stagnation point are $T = 300 \pm 30$ K in the cold flow and $T = 500 \pm 190$ K in the flow excited by the discharge in plenum. The uncertainty has been estimated as standard deviation of temperatures inferred from five pairs of NO PLIF images taken for each set of conditions. Higher uncertainty of stagnation temperature inferred in the flow excited by the discharge may be due to arc filaments in the discharge in plenum, which may result in "hot spot" formation in the flow. Although Joule heating of the flow in the discharge (see Fig. 12) contributes to higher stagnation point temperature with the discharge on, this result also suggests significant vibrational relaxation of nonequilibrium nitrogen flow, excited by the discharge in the nozzle plenum, behind the shock. Vibrational relaxation of the flow in the shock layer can be quantified by further measurements of nitrogen vibrational temperature behind the shock, using picosecond CARS diagnostics used in [11]. Temperature inferred in the freestream is subject to significant uncertainty due to very low fluorescence signal in this region in the $J = 16.5$ image (see Fig. 20). In the present work, the two rotational transitions were chosen for best temperature measurements sensitivity behind the bow shock. Note that temperature inferred in the "shadow" region below the cylinder model cannot be considered accurate, because laser beam lensing by the model may well cause saturation of the absorption transitions and result in a significant error in the temperature. Finally, temperature inferred in the wake behind the model cannot be inferred with any

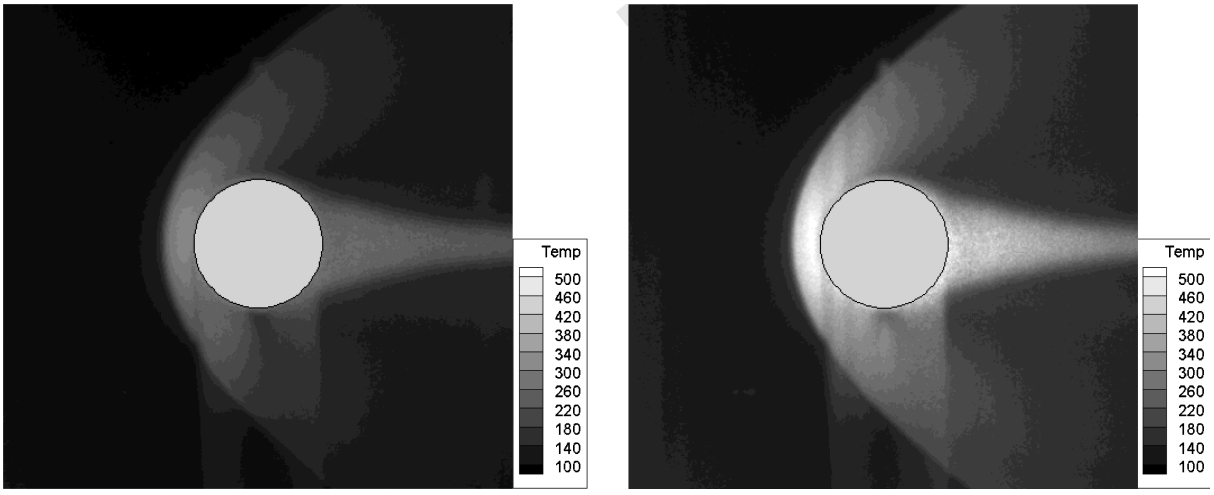

Fig. 21 Rotational temperature distributions inferred from NO PLIF images in Fig. 20. Left: no discharge, temperature at stagnation point $T = 300 \pm 30$ K. Right: with pulser sustainer discharge, temperature at stagnation point $T = 500 \pm 190$ K.

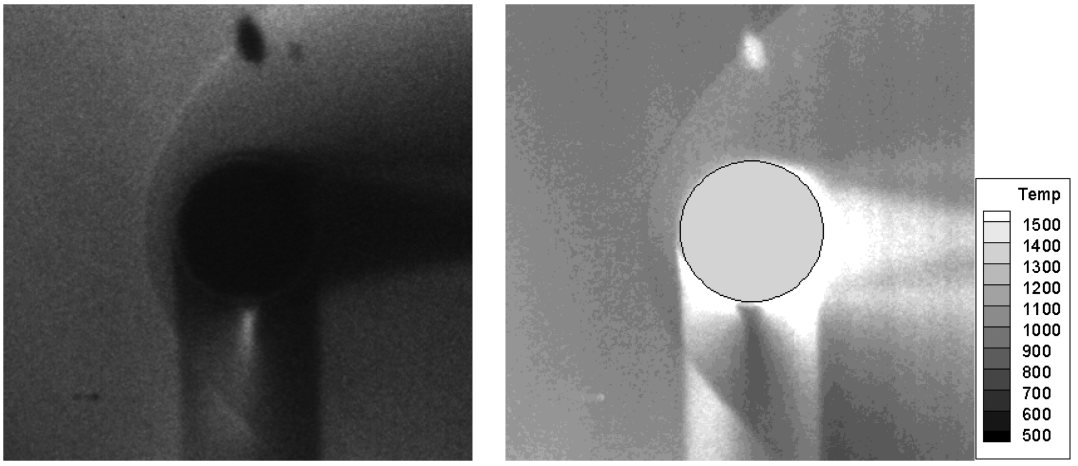

Fig. 22 Left: NO($v = 1$) PLIF image with pulser/dc discharge, 10 pulses integration. Right: vibrational temperature distribution. Free stream NO vibrational temperature T_V(NO) = 1000 ± 170 K.

certainty due to a very low fluorescence signal in this region, both in $J = 5.5$ and $J = 16.5$ images (see Fig. 20).

Figure 22a shows an NO PLIF image obtained when the pump laser was tuned to the NO absorption transition NO($X, v' = 1 \rightarrow A$, $v'' = 1$), $Q_{11} + P_{21}(J = 3.5)$ at 223.83 nm. The laser pulse-repetition rate was 10 kHz, and the image was accumulated over 10 laser pulses. The nitrogen flow at $P_0 = 370$ torr was excited by a pulser/sustainer discharge ($\nu = 100$ kHz, $U_{PS} = 4.5$ kV) and seeded with 0.3% of NO. In Fig. 22a, the $v' = 1$ fluorescence signal intensity near stagnation point is approximately 30 times lower compared to the fluorescence intensity of $v' = 0$ in the same region, shown in Fig. 20a. In nitrogen flows excited by the electric discharge in the nozzle plenum and seeded with small amounts of NO, bright spontaneous emission on NO($A^2\Sigma \rightarrow X^2\Pi$) transitions ($\gamma$ bands) was found to overlap with the NO PLIF signal due to rapid collisional energy transfer from the $N_2(A^3\Sigma)$ state generated in the discharge to the NO($A^2\Sigma$) state:

$$N_2(A^3\Sigma) + NO(X^2\Pi) \rightarrow N_2(X^1\Sigma) + NO(A^2\Sigma) \qquad (1)$$

with a room temperature rate coefficient of $k = 6.9 \cdot 10^{-11}$ cm^3/s [30]. However, the NO mole fraction of 0.3%, used to obtain the NO($v = 1$) PLIF image of Fig. 22a, appears sufficient to quench the $N_2(A^3\Sigma)$ state in the subsonic section completely, and no spontaneous emission of NO was detected at these conditions. Note that the intensity distribution in the NO($v = 1$) PLIF image is nearly uniform, indicating that NO vibrational temperatures in the freestream and behind the bow shock are fairly close.

Figure 22b shows a two-dimensional NO vibrational temperature distribution inferred from the intensity ratio of the NO PLIF images of Fig. 20a ($v' = 0$, $J = 5.5$) and Fig. 22a ($v' = 1$, $J = 3.5$), taking into account the difference in the laser pulse energies, Frank–Condon factors, rotational level populations, and Einstein coefficients for spontaneous emission. The average NO vibrational temperature inferred along the flow centerline in the freestream is T_V(NO)= 1000 K ± 170 K. Note that the apparent NO vibrational temperature exceeding 2000 K, inferred below the cylinder model (see Fig. 22b), are affected by low signal-to-noise ratio in this region (in the "shadow" of the model).

Figures 23 and 24 show split comparison of the temperature fields inferred from NO PLIF measurements with the CDF model predictions, with and without the pulser/dc discharge operating in plenum. For the conditions with the discharge on, comparison with CFD calculations was done for $T_0 = 500$ K and $T_{v0} = 1700$ K, close to the temperatures measured in plenum by picosecond CARS in

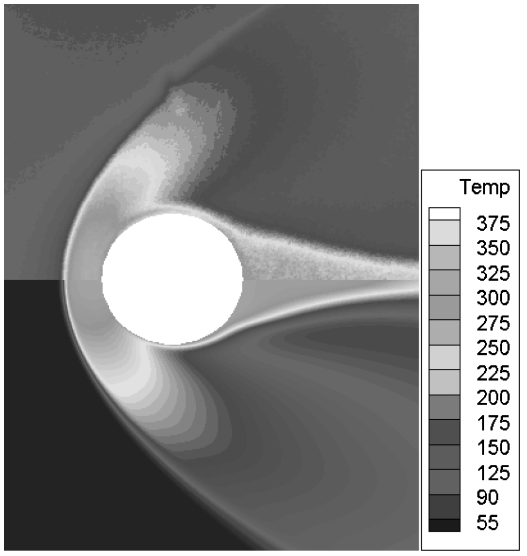

Fig. 23 Comparison of experimental (top) and CFD (bottom) temperature distributions for cold flow conditions (nitrogen, $P_0 = 370$ torr, $T_0 = 300$ K).

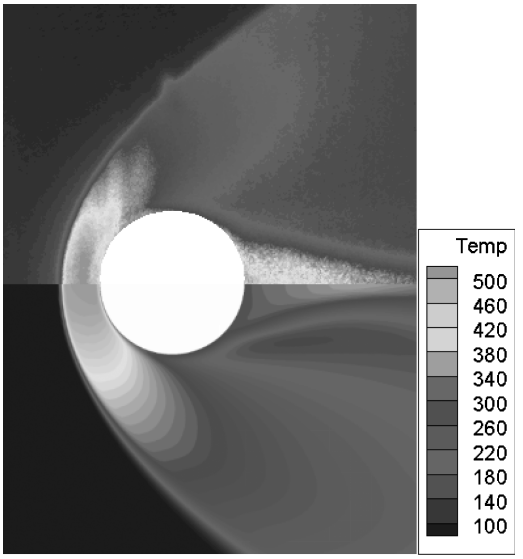

Fig. 24 Comparison of experimental (top) and CFD (bottom) temperature distributions with a with a pulsed/dc discharge operating in plenum ($\nu = 100$ kHz, $U_{PS} = 4.5$ kV). Nitrogen, $P_0 = 370$ torr. In the calculations, plenum conditions are $T_0 = 500$ K, $T_{v0} = 1700$ K.

our recent work [31]. As can be seen from Figs. 23 and 24, the results of NO PLIF thermometry measurements and CFD modeling-calculation predictions show good agreement. The results of the calculations also demonstrated that energy loaded by the discharge into the vibrational mode of nitrogen remains "frozen" throughout the entire flow, including flow behind the bow shock, consistent with the CARS measurements [31].

IV. Conclusions

In the present work, a small-scale Mach 5 wind tunnel with good flow quality, ample access for optical diagnostics, and ability to generate steady-state nonequilibrium flows was designed and operated. In the wind tunnel, transverse repetitively pulsed nanosecond discharge (peak voltage 25–30 kV, pulse duration 5 ns, pulse-repetition rate $\nu = 100$ kHz), fully overlapped with transverse dc discharge and operated at high plenum pressures ($P_0 =$ 0.5–1.0 atm), is used to load internal energy modes of nitrogen and oxygen molecules. The nanosecond pulse/dc discharge sustains stable diffuse plasmas in nitrogen at energy loadings of up to $\sim$0.1 eV/molecule (pulsed discharge power approximately 500 W, dc discharge power up to 2.7 kW), with most of the energy stored in the internal modes (vibrational and electronic). The wind tunnel generates nonequilibrium nitrogen and airflows with steady-state run time of 5–10 s, translational/rotational temperature of $T_0 \sim 300$–400 K, and estimated upper-bound nitrogen vibrational temperature of $T_{v0} \sim 2000$ K. Translational/rotational temperature in the discharge section was inferred from N_2 second positive system emission spectra. Nitrogen vibrational temperature downstream of the discharge section, predicted by kinetic-modeling calculations, is consistent with previous picosecond CARS measurements. Internal energy-mode disequilibrium in the flow excited in the discharge is controlled by injecting "rapid relaxer" species (carbon dioxide, nitric oxide, or hydrogen) into subsonic nonequilibrium flow between the discharge section and the nozzle throat.

Steady-state supersonic flow over a 5-mm-diam cylinder model placed in a Mach 5 test section is visualized by schlieren imaging and NO PLIF imaging, using an OSU-developed burst-mode laser. In the present work, the burst-mode laser was operated in the vicinity of 226 nm, at a pulse-repetition rate of 10–20 kHz, 10 pulses per burst, and pulse energy of $\sim$0.3 mJ/pulse. The laser was operated both in broadband and injection-seeded modes, generating narrow linewidth ($\sim$0.1 cm^{-1}) output in the latter case for single-line NO excitation in the flow. For NO PLIF measurements, nitric oxide was either injected into the nitrogen flow in the plenum or generated in a repetitively pulsed nanosecond discharge in dry air. Both single-pulse PLIF images and images integrated over 10–50 laser pulses have been obtained.

Single-line NO PLIF images on NO($X, v' = 0 \rightarrow A, v'' = 0$), $Q_{11} + P_{21}$ ($J = 5.5$), and $Q_{11} + P_{21}$ ($J = 16.5$) transitions are used to infer two-dimensional rotational temperature distributions in NO-seeded nitrogen flows in the supersonic test section. These measurements have been conducted in a cold flow (i.e., without the discharge in plenum) and in a flow vibrationally excited by the pulsed/dc discharge. NO PLIF signal intensities have been normalized on laser sheet intensity distributions on these two rotational transitions, which have been monitored during the measurements. Stagnation point temperature inferred in the vibrationally excited flow is significantly higher than that in the cold flow, $T = 500 \pm 190$ K versus $T = 300 \pm 30$ K, suggesting nitrogen vibrational relaxation in the shock layer. Single-line NO PLIF images on a NO($X, v' = 1 \rightarrow A, v'' = 1$) $Q_{11} + P_{21}$ ($J = 3.5$) transition have been used to infer the NO vibrational temperature in a nitrogen Mach 5 flow excited by the discharge in plenum and seeded with NO, $T_V(NO) = 1000 \pm 170$ K. The flowfield in the supersonic test section, with the cylinder model installed, is calculated by a three-dimensional compressible Navier–Stokes nonequilibrium flow code, showing good agreement with static pressure measurements, schlieren images, and NO PLIF images.

Ongoing work includes picosecond CARS measurements of rotational and translational temperatures in the plenum, in the freestream Mach 5 flow, and behind the bow shock. Along with high-frame-rate NO PLIF diagnostics used in the present work, picosecond CARS diagnostics forms a portable flow-characterization suite capable of taking detailed flow measurements at large-scale, pulsed hypersonic facilities, enhancing considerably their potential for flow characterization.

Acknowledgments

The present research is supported by the U.S. Air Force Office of Scientific Research Aerothermodynamics Program. The support and guidance of Eswar Josyula of the U.S. Air Force Research Laboratory is gratefully acknowledged.

References

[1] Leyva, I. A., Laurence, S., War-Kei Beierholm, A., Hornung, H. G., Wagnild, R., and Candler, G., "Transition Delay in Hypervelocity Boundary Layers by Means of CO_2/ Acoustic Instability Interactions," 47th AIAA Aerospace Sciences Meeting, Orlando, FL, AIAA Paper 2009-1287, Jan. 2009.

[2] Wagnild, R., Candler, G. V., Leyva, I. A., Jewell, J. S., and Hornung, H. G., "Carbon Dioxide Injection for Hypervelocity Boundary Layer Stability," 48th AIAA Aerospace Sciences Meeting, Orlando, FL, AIAA Paper 2010-1244, Jan. 2010.

[3] Josyula, E., "Oxygen Atoms' Effect on Vibrational Relaxation of Nitrogen in Blunt-Body Flows," *Journal of Thermophysics and Heat Transfer*, Vol. 15, No. 1, 2001, pp. 106–115. doi:10.2514/2.6585

[4] Nishihara, M., Takashima, K., Rich, J. W., and Adamovich, I. V., "Mach 5 Bow Shock Control by a Nanosecond Pulse Surface Dielectric Barrier Discharge," *Physics of Fluids*, Vol. 23,No. 6, 2011, pp. 066–101. doi: 10.1063/1.3599697

[5] Rich, J. W., Bergman, R. C., and Lordi, J. A., "Electrically Excited, Supersonic Flow Carbon Monoxide Laser," *AIAA Journal*, Vol. 13, No. 1, 1975, pp. 95–101. doi:10.2514/3.49636

[6] Generalov, N. A., Zimakov, V. P., Kosynkin, V. D., Raizer, Yu. P., and Roitenburg, D. I., "Method for Significantly Increasing the Stability Limit of the Discharge in Fast-Flow Large-Volume Lasers," *Soviet Technical Physics Letters*, Vol. 1, 1975, p. 201.

[7] Bruzzese, J. R., Hicks, A., Erofeev, A., Cole, A. C., Nishihara, M., and Adamovich, I. V., "Gain and Output Power Measurements in an Electrically Excited Oxygen-Iodine Laser with a Scaled Discharge," *Journal of Physics D: Applied Physics*, Vol. 43, No. 1, 2010, p. 015201. doi:10.1088/0022-3727/43/1/015201

[8] Nishihara, M., Jiang, N., Rich, J. W., Lempert, W. R., Adamovich, I. V., and Gogineni, S., "Low-Temperature Supersonic Boundary Layer Control Using Repetitively Pulsed MHD Forcing," *Physics of Fluids*, Vol. 17, No. 10, 2005, p. 106102. doi:10.1063/1.2084227

[9] Nishihara, M., Rich, J. W., Lempert, W. R., Adamovich, I. V., and Gogineni, S., "Low-Temperature $M = 3$ Flow Deceleration by Lorentz Force," *Physics of Fluids*, Vol. 18, No. 8, 2006, p. 086101. doi:10.1063/1.2265011

[10] Nishihara, M., Udagawa Takashima, K., Bruzzese, J. R., Adamovich, I. V., and Gaitonde, D., "Experimental and Computational Studies of Low-Temperature Mach 4 Flow Control by Lorentz Force," *Journal of Propulsion and Power*, Vol. 27, No. 2, 2011, pp. 467–476. doi:10.2514/1.49243

[11] Montello, A., Nishihara, M., Adamovich, I., Lempert, W. R., Barnat, E., and Kearney, S., "Picosecond CARS Measurements of Vibrational Distribution Functions in a Nonequilibrium Mach 5 Flow," 49th Aerospace Sciences Meeting and Exhibit, Orlando, FL, AIAA Paper 2011-1322, Jan. 2011; accepted for publication in *AIAA Journal*, 2012.

[12] Thurow, B., Jiang, N., Samimy, M., and Lempert, W., "Narrow-Linewidth Megahertz-Rate Pulse-Burst Laser for High-Speed Flow Diagnostics," *Applied Optics*, Vol. 43, No. 26, 2004, pp. 5064–5073. doi:10.1364/AO.43.005064

[13] Jiang, N., Webster, M., and Lempert, W. R., "New Advances in Generation of High Repetition Rate Burst Mode Laser Output," *Applied Optics*, Vol. 48, No. 4, 2009, pp. B23–B31. doi:10.1364/AO.48.000B23

[14] Jiang, N., and Lempert, W. R., "Ultra-High Frame Rate Nitric Oxide Planar Laser Induced Fluorescence imaging," *Optics Letters*, Vol. 33, No. 19, 2008, pp. 2236–2238. doi:10.1364/OL.33.002236

[15] Raizer, Yu. P., *Gas Discharge Physics*, Springer–Verlag, Berlin, 1991,

pp. 98–101, 421–431, Chaps. 5, 14.
[16] Chatelet, M., and Chesnoy, J., "New Results on the Vibrational Relaxation Time in Compressed Nitrogen at 293 K," *Chemical Physics Letters*, Vol. 122, No. 6, 1985, p. 550–552. doi:10.1016/0009-2614(85)87267-5
[17] Nompelis, I., Drayna, T. W., and Candler, G. V., "Development of Hybrid Unstructured Implicit Solver for the Simulation of Reacting Flows Over Complex Geometries," 34th AIAA Fluid Dynamics Conference and Exhibit, Portland, OR, AIAA Paper 2004-2227, June 2004.
[18] Nompelis, I., Drayna, T. W., and Candler, G. V., "A Parallel Unstructured Implicit Solver for Hypersonic Reacting Flow Simulations," 17th AIAA Computational Fluid Dynamics Conference, Toronto, AIAA Paper 2005-4867, June 2005.
[19] Druguet, M.-C., Candler, G. V., and Nompelis, I., "Effects of Numerics on Navier–Stokes Computations of Hypersonic Double-Cone Flows," *AIAA Journal*, Vol. 43, No. 3, 2005, pp. 616–623. doi:10.2514/1.6190
[20] Kim, S.-E., Makarov, B., and Caraeni, D., "A Multi-Dimensional Linear Reconstruction Scheme for Arbitrary Unstructured Grids," *16th AIAA Computational Fluid Dynamics Conference*, Orlando, FL, AIAA Paper 2003-3990, June 2003.
[21] Wright, M. J., Candler, G. V., and Bose, D., "Data-Parallel Line Relaxation Method for the Navier–Stokes Equations Using Gauss-Seidel Line Relaxation," *AIAA Journal*, Vol. 36, No. 9, 1998, pp. 1603–1609. doi:10.2514/2.586
[22] Wright, M. J., Candler, G. V., and Prampolini, M., "Data-Parallel Lower Upper Relaxation Method for the Navier–Stokes Equations," *AIAA Journal*, Vol. 34, No. 7, 1996, pp. 1371–1377. doi:10.2514/3.13242
[23] Candler, G. V., "Hypersonic Nozzle Analysis Using an Excluded Volume Equation of State," 38th AIAA Thermophysics Conference, Toronto, AIAA Paper 2005-5202, June 2005.
[24] Nishihara, M., and Adamovich, I. V., "Numerical Simulation of a Crossed Pulser-Sustainer Discharge in Transverse Magnetic Field," *IEEE Transactions on Plasma Science*, Vol. 35, No. 5, 2007, pp. 1312–1324. doi: 10.1109/TPS.2007.906440
[25] Roux, F., Michaud, F., and Vervloet, M., "High Resolution Fourier Spectrometry of $^{14}N_2$ Violet Emission Spectrum: Extensive Analysis of the $C^3\Pi_u - B^3\Pi_g$ System," *Journal of Molecular Spectroscopy*, Vol. 158, No. 2, 1993, pp. 270–277. doi:10.1006/jmsp.1993.1071
[26] Budo, A., "Intensitatsformeln fur die Triplettbanden," *Zeitschrift fur Physik D: Atoms, Molecules and Clusters*, Vol. 105, 1937, pp. 579–587. doi: 10.1007/BF01371563
[27] Huxley, L. G. H., and Crompton, R. W., *The Diffusion and Drift of Electrons in Gases*, Wiley, New York, 1974, Chaps. 2–4.
[28] Itikawa, Y., Hayashi, M., Ichimura, A., Onda, K., Sakimoto, K., Takayanagi, K., Nakamura, M., Nishimura, H., and Takayanagi, T., "Cross Sections for Collisions of Electrons and Photons with Nitrogen Molecules," *Journal of Physical and Chemical Reference Data*, Vol. 15, No. 3, 1986, pp. 985–1010. doi:10.1063/1.555762
[29] Uddi, M., Jiang, N., Adamovich, I. V., and Lempert, W. R., "Nitric Oxide Density Measurements in Air and Air/Fuel Nanosecond Pulse Discharges by Laser Induced Fluorescence," *Journal of Physics D: Applied Physics*, Vol. 42, No. 7, 2009, p. 075205. doi:10.1088/0022-3727/42/7/075205
[30] Guerra, V., Sa, P. A., and Loureiro, J., "Role Played by the $N_2(A^3\Sigma_u^+)$ Metastable in Stationary N_2 and N_2–O_2 Discharges", *Journal of Physics D: Applied Physics*, Vol. 34, 2001, pp. 1745–1755. doi:10.1088/0022-3727/34/12/301
[31] Montello, A., Nishihara, M., Rich, J. W., Adamovich, I., and Lempert, W. R., "Picosecond USED-CARS for Simultaneous Rotational/Translational and Vibrational Temperature Measurement of Nitrogen in a Nonequilibrium Mach 5 Flow," 50th Aerospace Sciences Meeting, Nashville, TN, AIAA Paper 2011-0239, Jan. 2012.

G. Elliott
Associate Editor